

# A Nonmonotonic Precipitation Response to Changes in Soil Moisture in the Presence of Vegetation

ARYEH J. DRAGER,<sup>a,b</sup> LEAH D. GRANT,<sup>a</sup> AND SUSAN C. VAN DEN HEEVER<sup>a</sup>

<sup>a</sup> Colorado State University, Fort Collins, Colorado

<sup>b</sup> University of Nebraska–Lincoln, Lincoln, Nebraska

(Manuscript received 3 June 2021, in final form 11 March 2022)

**ABSTRACT:** In many parts of the world, humans rely on afternoon rainfall for their water supply. However, it is not fully understood how land surface properties influence afternoon precipitation. In fact, disagreement remains regarding the relative prevalence of “wet-soil advantage” regimes, in which wet soils receive more precipitation than do dry soils, and “dry-soil advantage” regimes, in which the opposite occurs. Recent studies have proposed that the permanent wilting point (PWP) soil moisture threshold influences the location and organization of convective clouds. Motivated by this work, we investigate how changes in soil moisture relative to the PWP affect the timing and amount of surface rainfall, as well as how this response depends on the presence or absence of vegetation. This investigation is carried out by conducting several series of high-resolution, idealized numerical experiments using a fully coupled, interactive soil–vegetation–atmosphere modeling system. From these experiments, a new soil moisture–precipitation relationship emerges: in the presence of vegetation, simulations with moderately dry soils, whose initial liquid water content slightly exceeds the PWP, generate significantly less surface precipitation than do those with the driest or wettest soils. This result suggests that simulated wet-soil advantage and dry-soil advantage regimes may not necessarily be mutually exclusive, insofar as extremely wet and extremely dry soils can both exhibit an advantage over moderately dry soils. This nonmonotonic soil moisture–precipitation relationship is found to result from the PWP’s modulation of transpiration of water vapor by plants. In the absence of vegetation, a wet-soil advantage occurs instead in these idealized simulations.

**SIGNIFICANCE STATEMENT:** This modeling study suggests a new type of rainfall response to soil moisture in which intermediate-moisture soils receive less rainfall than do the driest or wettest soils. Previous studies have suggested that afternoon rainfall, which impacts populations across the globe, consistently increases or decreases with increasing soil moisture; our results suggest that this relationship can instead be nonmonotonic under certain conditions. This nonmonotonic response only occurs in the presence of vegetation, suggesting that plants play a key role in determining the soil moisture dependence of afternoon precipitation. In examining the mechanisms behind these trends, we shed light on interactions between soil, vegetation, the boundary layer, and clouds that coarse-resolution models may fail to capture.

**KEYWORDS:** Vegetation-atmosphere interactions; Convective clouds; Precipitation; Rainfall; Atmosphere-land interaction; Soil moisture; Cloud resolving models

## 1. Introduction

In Earth’s climate system, soil moisture and precipitation are inextricably linked as part of a broader global hydrologic cycle (Rodell et al. 2015). The coupling between soil moisture, vegetation, and precipitation exhibits multiple layers of complexity. At the simplest level, water escapes from the soil into the atmosphere via evapotranspiration (combined transpiration by plants, evaporation of liquid water from the soil surface, and evaporation of precipitation intercepted by plants or other canopy objects) (Hillel 2003; Berg and Sheffield 2019). Once in the atmosphere, it is able eventually to condense and return to the soil in the form of precipitation (Hillel 2003; Eltahir and Bras 1996). However, this recycling between the soil, vegetation, and atmosphere does not necessarily guarantee that increases in soil moisture will yield local or widespread enhancements in precipitation. Indeed, multiple

studies over the past several decades have identified “dry-soil advantage” scenarios, in which the atmosphere produces more local rainfall over dry soils than over wet soils (Giorgi et al. 1996; Cheng and Cotton 2004; Taylor et al. 2012; Yuan et al. 2020), as well as “wet-soil advantage” scenarios, in which the reverse is true (Findell and Eltahir 1997; Eltahir 1998; Findell et al. 2011; Schlemmer et al. 2012). Several additional studies have suggested mixed outcomes, with dry-soil advantages and wet-soil advantages each occurring under different conditions (Findell and Eltahir 2003a; Ford et al. 2015a,b; Tuttle and Salvucci 2016).

The processes governing the response of rainfall to soil moisture and vegetation, such as boundary layer growth and the development of convective clouds, are not explicitly represented in most coarse-resolution global models (Randall et al. 2003). Instead, both weather forecasts and climate predictions rely on parameterizations that are designed to capture the essential aspects of the various processes while remaining computationally efficient. The limitations of these parameterizations, such as their difficulty reproducing the

Corresponding author: Aryeh J. Drager, aryeh.drager16@alumni.colostate.edu

DOI: 10.1175/JHM-D-21-0109.1

© 2022 American Meteorological Society. For information regarding reuse of this content and general copyright information, consult the [AMS Copyright Policy](#) ([www.ametsoc.org/PUBSReuseLicenses](#)).

observed diurnal cycle of precipitation (Baranowski et al. 2018; Rio et al. 2009; Dirmeyer et al. 2012), which is critical to Earth's water and energy balances, are well documented and highlight the need for improved process-level understanding. Enhanced process-level understanding of the soil moisture–precipitation relationship will not only improve confidence in model projections of Earth's hydrologic cycle and conditions such as drought, but also enable the formulation of strategies for optimizing the efficiency of agricultural land-use decisions and practices such as irrigation (Lawston 2017).

Previous studies have used several different approaches to investigating soil moisture–precipitation interactions. These include analytic and simple numerical models (Gentine et al. 2013; Findell and Eltahir 2003b); one-dimensional models (Ek and Mahrt 1994; Ek and Holtslag 2004); global and regional Earth system models with parameterized convection and land surfaces (Koster et al. 2004; Hohenegger et al. 2009); regional convection-permitting model simulations, which begin to resolve convective motions (Hohenegger et al. 2009); and high-resolution large-eddy simulations, which resolve convective clouds and begin to resolve turbulent eddies (Cioni and Hohenegger 2017; Chlond et al. 2014; Kristianti et al. 2018; Kang 2016; Drager et al. 2020). Observational work assessing statistical relationships between soil moisture and precipitation has also been performed (Yuan et al. 2020; Findell and Eltahir 1997; Ford et al. 2015b; Guillod et al. 2015). While observational studies are critical for evaluating the physical processes involved, one important limitation inherent to observational work is that it is impossible to conduct controlled experiments in which only one parameter (e.g., soil moisture) is changed at a time. As a result, inferring causality is not straightforward (Santanello et al. 2018; Tuttle and Salvucci 2016). Another limitation is that key physical parameters, such as soil texture and soil moisture, are heterogeneous and difficult to measure (Mohanty and Zhu 2007). Even when measurements are available, there is no guarantee that they will be representative of their surroundings (Nicolai-Shaw et al. 2015). By contrast, numerical models provide a complete spatiotemporal record of the events being simulated, and model-derived process rates allow diagnosis of physical mechanisms. The present investigation is conducted using an idealized numerical modeling approach. In this approach, interpretability is maximized by minimizing complicating factors and confounding variables. The problem of interest is simplified to its bare essence, and it can become possible to draw robust conclusions.

Soil moisture helps to control the amount of water available for evapotranspiration (Stull 1988). For a given amount of incoming solar radiation (hereafter *insolation*), and for a given amount of heat flux into the ground, surface energy balance requires that increases in evapotranspiration (surface latent heat fluxes) be accompanied by compensating decreases in surface sensible heat fluxes and surface emission of longwave radiation (Stull 1988). When the soil is dry, evapotranspiration is suppressed, and insolation results in substantial daytime warming of the uppermost layer of soil, which in turn supports strong sensible heat fluxes into the atmosphere (Stull 1988).

Two recent studies (Drager et al. 2020; Hohenegger and Stevens 2018) have drawn attention to a particular threshold in soil moisture–convection interactions that may directly affect evapotranspiration and therefore surface energy balance as a whole: the permanent wilting point (PWP). The PWP is, for a given soil texture, the amount of soil moisture below which typical plants' roots are unable to remove any liquid water from the soil (Hillel 2003). Soils drier than the PWP hold onto their water too tightly for root uptake of water, and as a result, transpiration by plants shuts down. In Hohenegger and Stevens (2018), it was found using idealized convection-permitting modeling that spatial differences in soil moisture, where one region is moister than the PWP and an adjacent region is drier, induce a moist region-to-dry region flow that initiates convection over the dry region, in agreement with the earlier observational study by Taylor et al. (2011). It was found in the large-eddy simulations of Drager et al. (2020) that as the initialization soil moisture decreases to levels below the PWP, the character of convective cold pools (Drager and van den Heever 2017) changes abruptly and dramatically. However, this study did not probe surface rainfall accumulations. In further examining the simulations of Drager et al. (2020), we have found that the amount of domain-mean accumulated precipitation is substantially lower for initialization soil moistures that are just above the PWP than for very moist or very dry soils. The present work seeks to examine this non-monotonic soil moisture–precipitation relationship, with a specific focus on how this relationship relates to the PWP.

In particular, the present study is guided by the following question: How does the PWP modulate the precipitation response to changes in soil moisture, and how does this modulation depend on the characteristics of the land surface? Based on results from the simulations performed in Drager et al. (2020), a decrease in precipitation is expected for soils just slightly moister than the PWP. But what physical processes drive this trend in precipitation? Furthermore, Drager et al. (2020) examines only a single soil texture and land covering type, with five initial soil moistures. The present study seeks to sample the soil texture, land cover, and soil moisture parameter space more comprehensively in order to elucidate the physical mechanisms behind the described precipitation response.

## 2. Methods

High-resolution, cloud-resolving model simulations are performed using the open-source Regional Atmospheric Modeling System (RAMS), version 6.2.10 (Cotton et al. 2003; Saleeby and van den Heever 2013; van den Heever et al. 2021), which is fully coupled to the Land Ecosystem–Atmosphere Feedback, version 3 (LEAF-3) soil–vegetation–atmosphere transfer scheme (Lee 1992; Walko et al. 2000; Walko and Tremback 2005). The LEAF-3 scheme models the vegetated near-surface environment using a greenhoused canopy framework (following the terminology of Goudriaan 1989; see also Lee 1992). A layer of canopy air exists in which vegetation is embedded, and there are distinct vegetation temperatures and canopy air temperatures. LEAF-3 also contains a soil model with a user-specified number of soil

layers, each with its own volumetric soil moisture and temperature. The volumetric soil moisture and temperature at each 3D soil grid point are prognosed according to fluxes of sensible heat, latent heat, radiation, and precipitation. Fluxes of sensible and latent heat are parameterized using a voltage-resistance approach. Direct surface evaporation follows [Mission Research Corporation \(1997\)](#), evaporation of canopy-intercepted precipitation follows [Walko et al. \(2000\)](#), and transpiration follows [Lee \(1992\)](#). LEAF-3 and its predecessors have been used successfully in prior studies of soil moisture impacts on precipitation (e.g., [Cheng and Cotton 2004](#); [Park et al. 2020](#); [Suarez et al. 2014](#)).

Direct surface evaporation from the top soil level into the atmosphere is driven by the difference between the soil–surface water vapor mixing ratio  $r_{v,sfc}$  and the canopy–air water vapor mixing ratio  $r_{v,canopy}$ . Following [Mission Research Corporation \(1997\)](#), the value of  $r_{v,sfc}$  is calculated by combining formulas from [Philip \(1957\)](#) and [Lee and Pielke \(1992\)](#). Transpiration is controlled by a stomatal conductance that depends on carbon dioxide availability, photosynthetically active radiation (based on insolation), temperature, and water stress. The water stress has contributions both from soil moisture and from the humidity of the near-surface air ([Lee 1992](#)), and since LEAF-3 does not track carbon dioxide concentrations, it is assumed that sufficient carbon dioxide is always available. To calculate stomatal conductance, a vegetation-type-dependent base stomatal conductance is then multiplied by several factors ranging from 0 to 1, each representing one of the processes that modulate stomatal conductance. Changes in the stomatal conductance occur gradually, with a built-in  $e$ -folding time scale of 15 min. The transpiration process extracts water from whichever soil layer in the root zone has the greatest soil water potential.

As in [Cioni and Hohenegger \(2017\)](#), the horizontal grid spacing of the numerical experiments is 250 m, and the horizontal dimensions of each simulation’s domain are 100 km  $\times$  100 km. The lateral boundary conditions are periodic. The vertical grid spacing increases from 40 m near the surface to 250 m aloft with a stretch ratio of 1.025 and a total of 127 vertical levels. Each simulation is run from 0700 to 2100 local time (LT), so as to capture a single afternoon’s cycle of convective cloud formation and decay, with insolation based on a latitude of 18.18°N on 2 August 2010. The LEAF-3 land surface contains 11 soil layers extending to a depth of 0.5 m, and the initial soil temperatures are slightly warmer than the lowest level of the atmosphere, following [Drager et al. \(2020\)](#) and [Grant and van den Heever \(2014\)](#).

This research is undertaken in conjunction with the Office of Naval Research’s Propagation of Intra-Seasonal Tropical Oscillations (PISTON) field campaign, one of whose goals is improve our understanding of land–ocean–atmosphere interactions over the Philippine archipelago. Simulations are initialized with a modified morning sounding ([Fig. 1](#)) from the Laoag site on the island of Luzon in the Philippines, and the initial state (including soil and vegetation properties) is horizontally homogeneous except for pseudorandom thermal perturbations in the lowest  $\sim$ 520 m of the atmosphere, following [Drager et al. \(2020\)](#). Initial winds are calm. The

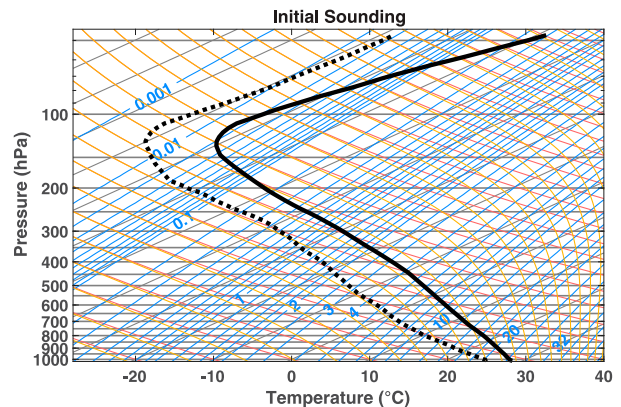


FIG. 1. The initial sounding for all simulations, plotted on a skew  $T$ - $\log p$  diagram. The solid black line is the temperature, and the broken black line is the dewpoint temperature. The labels on the blue lines indicate water vapor mixing ratio ( $\text{g kg}^{-1}$ ).

initial horizontal homogeneity implies that some aspects of the soil moisture–precipitation relationship discussed by [Taylor et al. \(2011, 2012\)](#), such as enhancement of precipitation over mesoscale patches of drier soil, will not be captured in these simulations. Smaller-scale heterogeneities in soil moisture and other soil and atmospheric properties do emerge as each simulation evolves.

[Findell and Eltahir \(2003b\)](#) introduced the CTP- $\text{HI}_{\text{low}}$  framework for predicting whether a *wet-soil* or *dry-soil advantage* regime is likely based on the properties of the early morning profiles of temperature and humidity. When their methods are applied to the initial sounding, values of  $\text{CTP} = 204 \text{ J kg}^{-1}$  and  $\text{HI}_{\text{low}} = 10.6 \text{ K}$  are obtained, where CTP is the convective triggering potential and  $\text{HI}_{\text{low}}$  is a low-level humidity index. According to the CTP- $\text{HI}_{\text{low}}$  framework, these indices place the sounding in a dry-soil advantage regime but near a transition zone (in the CTP- $\text{HI}_{\text{low}}$  plane) between wet-soil advantage and dry-soil advantage regimes.

Other aspects of the model setup are generally identical to those in [Drager et al. \(2020\)](#). Of these, we note that the RAMS two-moment, bin-emulating microphysics scheme with eight hydrometeor classes is used ([Saleeby and van den Heever 2013](#); [Meyers et al. 1997](#); [Saleeby and Cotton 2004, 2008](#)). The LEAF-3 scheme has sophisticated interactions with the microphysics scheme. Precipitation landing on the surface is able to be intercepted by both vegetation and soil, and the rain mass and internal energy (temperature) are incorporated into the prognosed soil moisture and temperature. We also employ the two-stream radiative transfer scheme of [Harrington \(1997\)](#), with radiative fluxes and heating rates updated every 300 s, as well as a modified form of the Smagorinsky turbulence parameterization ([Drager et al. 2020](#); [Smagorinsky 1963](#); [Hill 1974](#)). There is no topography or Coriolis acceleration. The Robert–Asselin–Williams time filter ([Williams 2009](#)) is used in order to improve the numerical accuracy of the simulations.

We perform 40 simulations, each representing a unique combination of soil type (silty clay loam or clay loam), land

cover type (bare soil or wooded grassland), and soil moisture (25%, 40%, 45%, 50%, 55%, 60%, 65%, 70%, 75%, or 95% of soil saturation). Wooded grassland occupies much of Luzon, and the bare-soil simulations are conducted in order to assess the role of vegetation. The soil moisture values are chosen in order to examine the entire soil moisture spectrum, from very dry to very moist, and a fine soil moisture interval of 5% is used over 40%–75% in order to provide high sampling resolution for soil moistures ranging from just below the PWP to just above the field capacity. Silty clay loam and clay loam are chosen because, as formulated in LEAF-3, they have similar saturation values of volumetric soil moisture (0.477 and 0.476  $\text{m}^3 \text{m}^{-3}$ , respectively) and field capacity (0.322 and 0.325  $\text{m}^3 \text{m}^{-3}$ , respectively) but substantially different PWPs (nominally 0.218 and 0.250  $\text{m}^3 \text{m}^{-3}$ , respectively). Both soil types are prominent in Luzon according to the RAMS soil type database. Therefore, by testing these two soil types, we are able to vary PWP while approximately controlling for field capacity and saturation volumetric soil moisture, without substantial loss of realism. The PWP and field capacity in LEAF-3 are not specified but are rather calculated based on other soil parameters prescribed for each soil texture. This fact has two important implications: 1) it would be impractical and potentially unrealistic to hold saturation volumetric soil moisture and field capacity values precisely constant while varying only the PWP, and 2) the two soil types examined here have other differences that influence processes such as heat and moisture conduction beyond the three parameters discussed here, and therefore we can expect variation between simulations with different soil textures beyond that attributable to differences merely in field capacity and PWP.

The grid spacing used in these numerical experiments is sufficient to begin to resolve the largest turbulent eddies (Bryan et al. 2003) but may be insufficient to resolve fully some of the shallow clouds produced in these simulations, as well as convective cold pool dissipation processes (Grant and van den Heever 2016). The experiments of Drager et al. (2020), however, used a finer horizontal grid spacing of 125 m. Although they were performed with an earlier version of RAMS, those simulations used a wooded grassland, silty clay loam land surface, and they produced a soil moisture–precipitation relationship qualitatively similar to that obtained for the present study’s corresponding wooded grassland, silty clay loam simulations.

### 3. Results

#### a. Overall results

Figure 2 shows the total domain-mean accumulated rainfall over the course of each simulation, as a function of initial soil moisture saturation fraction. The four curves correspond to the four series of simulations outlined in section 2: 1) wooded grassland and silty clay loam soil, 2) wooded grassland and clay loam soil, 3) bare silty clay loam soil, and 4) bare clay loam soil. In the discussion that follows, each simulation will be referred to as S#M%,

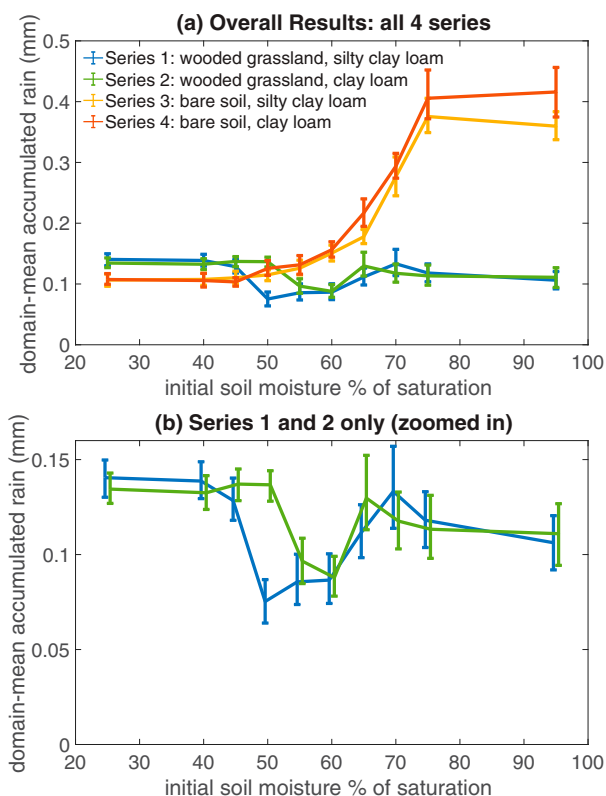


FIG. 2. (a) The domain-mean accumulated rainfall, as a function of initial soil moisture, at the end of each of the 40 simulations. Error bars indicate 95% confidence intervals for the mean calculated using the approach described in appendix B. (b) Zoomed-in view of (a), showing the Series 1 and Series 2 data only. The two curves are shifted slightly in the horizontal in order to improve readability.

where # is the series number (1–4) and % is the initial soil saturation percentage (e.g., S3M25 is the Series 3 simulation initialized with soil moisture at 25% of saturation). Series 1 and 2, in which vegetation is present, exhibit qualitatively similar variation in accumulated rainfall as a function of initial soil moisture, as do Series 3 and 4, in which vegetation is absent. In all four series of simulations, precipitation has limited sensitivity to soil moisture for the driest and wettest soil moisture initializations. The domain-mean precipitation totals, which incorporate many grid points receiving no precipitation, are quite low (tenths of millimeters). Despite the low domain-mean precipitation totals, every simulation contains individual grid points that receive more than 3 mm ( $\sim 0.12$  in.) of rainfall by 2100 LT, which is well above the threshold of being considered “measurable” (as is discussed further below).

When vegetation is absent (Series 3 and 4), rainfall increases nearly monotonically with increasing soil moisture. By contrast, when vegetation is present (Series 1 and 2), the curves’ interiors are V-shaped, with the least rainfall occurring for midrange initial soil moisture values. As will be discussed later, the local minima in Series 1 and Series 2 occur

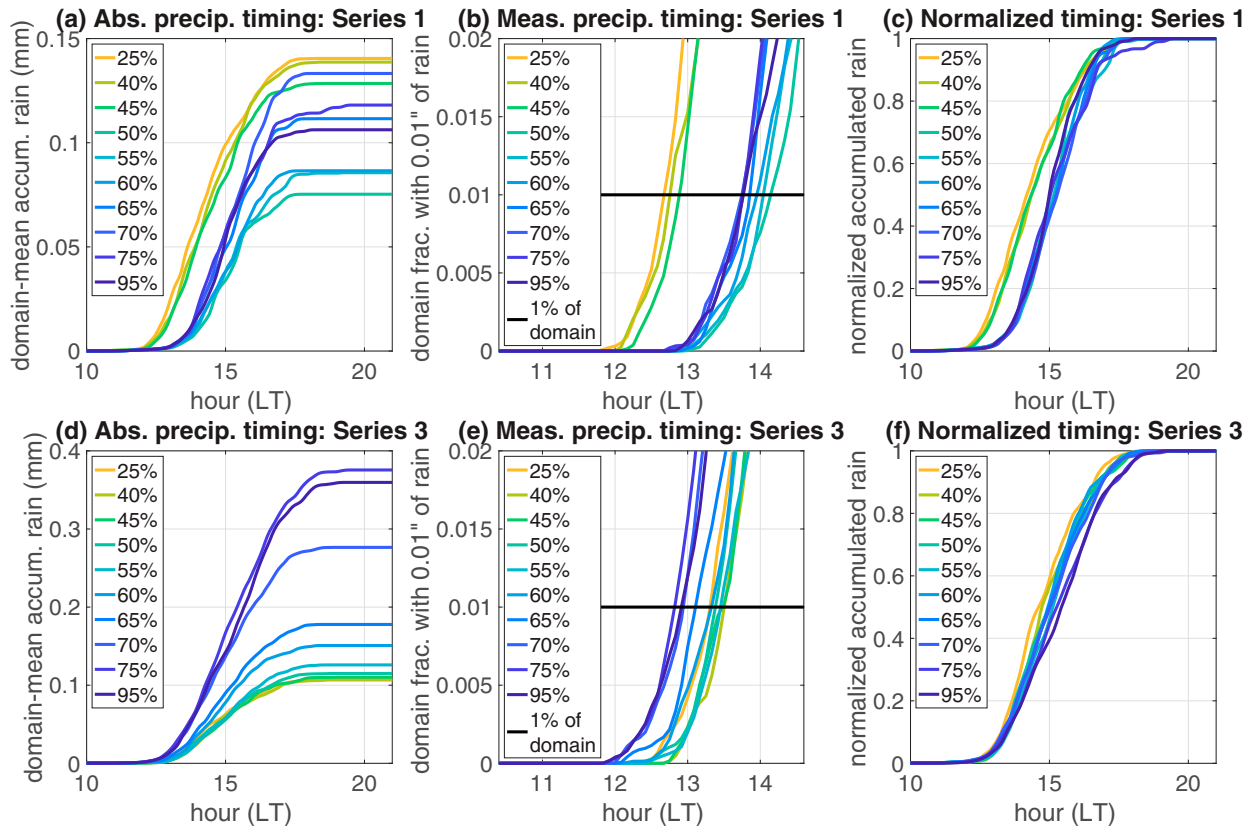


FIG. 3. Precipitation timing for (a)–(c) Series 1 (wooded grassland, silty clay loam) and (d)–(f) Series 3 (bare soil, silty clay loam). Each curve corresponds to a single simulation whose initial soil moisture (fraction of saturation) is indicated by the legend. The permanent wilting point is 45.7% for these simulations. Panels (a) and (d) show the horizontal-mean amount of rain that has accumulated at the surface between the start of the simulation and a given time. Panels (b) and (e) show the fraction of grid points that have accumulated measurable rainfall (defined as 0.01 in., or 0.254 mm) between the start of the simulation and a given time. Finally, (c) and (f) show the same curves as in (a) and (d), respectively, except that each curve is normalized by the amount of rain that has fallen by the end of the corresponding simulation. Note that the horizontal axis limits in (b) and (e) differ from those in the other four panels.

for values slightly moister than the respective soil types’ PWP. Throughout this study, we use the term *intermediate* to describe these midrange soil moistures that are slightly above the PWP. It should be noted, however, that soil moistures drier than the PWP generally do not occur in vegetated areas. Therefore, these “intermediate” soil moistures are actually at the drier end of what may be considered realistic. Nevertheless, multiple prior investigations of the soil moisture–precipitation relationship have considered soil moistures well below the PWP (Findell and Eltahir 2003b; Gero and Pitman 2006; Grant and van den Heever 2014; Park et al. 2020; Ramos da Silva and Avissar 2006). We hold that, in the context of idealized studies such as this one, including these potentially unrealistically dry parts of the soil moisture parameter space can help to elucidate the physical processes that govern the soil moisture–precipitation relationship.

The initial soil moisture in these simulations affects not only total precipitation accumulation, but also precipitation timing. Figure 3a shows time series of domain-mean accumulated rainfall for all 10 simulations in Series 1 (wooded grassland, silty clay loam). Between 1200 and 1600 LT, the curves are

clustered into three main groups: the driest-soil simulations (S1M25, S1M40, and S1M45 of saturation), the wettest-soil simulations (S1M65, S1M70, S1M75, and S1M95), and finally the intermediate-soil-moisture simulations (S1M50, S1M55, and S1M60). There are multiple ways to conceptualize and quantify precipitation timing, with different implications for weather and climate. Figure 3b focuses on the timing of measurable precipitation across the domain, where measurable precipitation is defined following the National Weather Service threshold of 0.254 mm (0.01 in.) of surface accumulation (NWS 2009). If we consider the time necessary for 1% of the domain area to receive measurable precipitation, a metric which is perhaps best suited to weather and agricultural applications, we find that the driest-soil simulations reach the threshold first, the wettest-soil simulations reach the threshold over an hour later, and the S1M50 simulation reaches this threshold about 25 min later than do the wettest-soil simulations. However, if we consider normalized precipitation timing (Fig. 3c), in which each curve in Fig. 3a is divided by its value at 2100 LT, the delay in precipitation onset in the intermediate-soil-moisture simulations relative to the wettest-soil simulations disappears.

We might therefore conclude that for climate applications concerned with the diurnal cycle, there are only two groups: the driest-soil simulations and the combined intermediate-soil-moisture and wettest-soil simulations.

The corresponding time series for Series 2 (wooded grassland, clay loam; not shown) behave qualitatively similarly to the Series 1 time series, although in Series 2 there is no systematic delay in the intermediate-soil-moisture simulations' onset of precipitation relative to the wettest-soil simulations' onset of precipitation. In Series 3 (bare soil, silty clay loam; Figs. 3d–f) and Series 4 (bare soil, clay loam; not shown), wet soils generally exhibit an earlier onset of precipitation than do dry soils from a “measurable precipitation” perspective (Fig. 3e) but not from a “normalized” perspective (Fig. 3f).

In summary, with respect to total accumulated precipitation, Series 1 and Series 2 (vegetated) exhibit an *intermediate-soil-moisture disadvantage*, in which intermediate-moisture soils yield the least precipitation. Series 3 and Series 4 (nonvegetated) exhibit a wet-soil advantage. Results pertaining to precipitation timing broadly depend on the metric used to define precipitation onset.

### b. Simulations with vegetation

When dense vegetation is present, as in Series 1 and Series 2, transpiration plays a significant role. By contrast, when vegetation is absent, as in Series 3 and Series 4, there is no transpiration, and therefore all surface latent heat fluxes occur via evaporation from the top soil level into the atmosphere. In the land surface model, as in nature, transpiration and evaporation are governed by different factors (see section 2). Figure 4a shows how transpiration depends on soil moisture for both the silty clay loam and clay loam soil types. Below each soil type's PWP, the multiplicative factor is very close to 0. Above the PWP, the factor sharply increases to nearly unity. Therefore, transpiration is a strong function of soil moisture via the soil moisture–based water stress control on stomatal conductance.

Figure 4b shows how the soil–surface water vapor mixing ratio  $r_{v,sfc}$  depends on soil moisture for representative values that we have prescribed (for illustration purposes) of  $r_{v,canopy}$ , surface temperature, and surface pressure (see section 2 for discussion of the significance of  $r_{v,sfc}$  and  $r_{v,canopy}$ ). Note that  $r_{v,sfc}$  is essentially constant above the field capacity, which is nearly identical for the silty clay loam and clay loam soil textures, and approaches the graph's prescribed  $r_{v,canopy}$  value of  $20 \text{ g kg}^{-1}$  for saturation fractions below  $\sim 0.2$  (20%). In the latter case, there is no humidity gradient between the surface and canopy. In between these two extremes, there is a gradual transition in direct surface evaporation from dry soils to wet soils. This transition contrasts with that for stomatal conductance, which more closely resembles a step function centered near the PWP.

### c. Examination of Series 1 (wooded grassland, silty clay loam)

Figures 5 and 6 show several horizontal-mean, temporally averaged quantities as a function of initial soil moisture for all

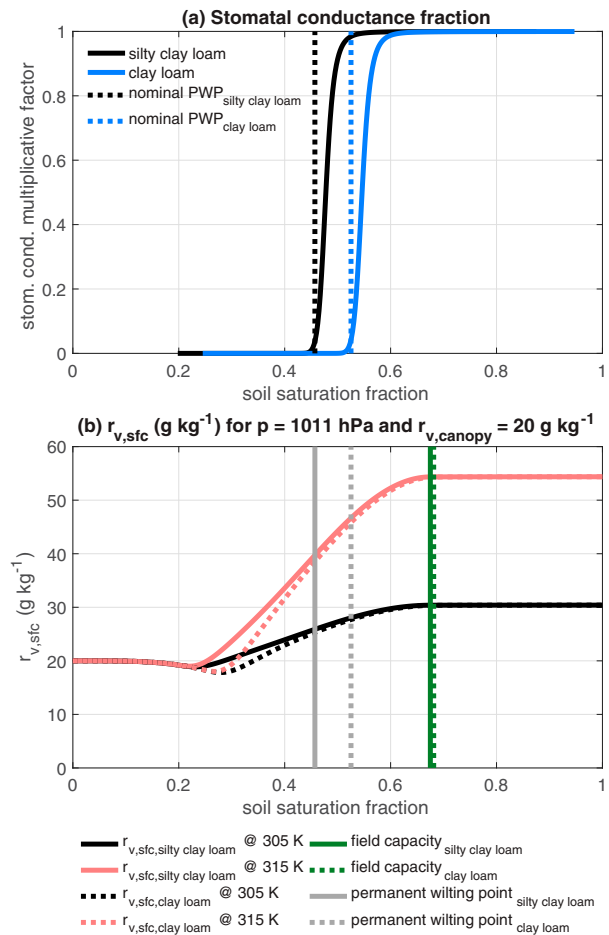


FIG. 4. Controls on evapotranspiration in the LEAF-3 soil–vegetation–atmosphere transfer scheme. Panel (a) shows the extent to which soil moisture limits transpiration, via a multiplicative factor that ranges from 0 (no transpiration allowed) to 1 (soil moisture does not limit stomatal conductance). The PWP for silty clay loam is 45.7% of saturation, and the PWP for clay loam is 52.5% of saturation. Panel (b), which relates to bare-soil evaporation, shows the soil moisture dependence of the soil–surface water vapor mixing ratio  $r_{v,sfc}$  for surface pressure  $p_{sfc} = 1011 \text{ hPa}$ , canopy water vapor mixing ratio  $r_{v,canopy} = 20 \text{ g kg}^{-1}$ , and top soil layer temperature at two arbitrary sample temperatures:  $T_{sfc} = 305 \text{ K}$  (black) and  $T_{sfc} = 315 \text{ K}$  (light red).

four series of simulations. In this section, we will focus on Series 1 (blue).

#### 1) SURFACE HEAT FLUXES IN SERIES 1 ARE LARGELY CONTROLLED BY THE PWP AND FIELD CAPACITY

Starting from the beginning of each simulation, the factor that immediately acts to distinguish the drier-soil simulations from the wetter-soil simulations is the soil moisture component of the water stress. The stomatal conductance is much greater in the seven wettest-soil simulations than in the three driest-soil simulations (Fig. 5a). The threshold separating the group of three dry-soil simulations from the group of seven

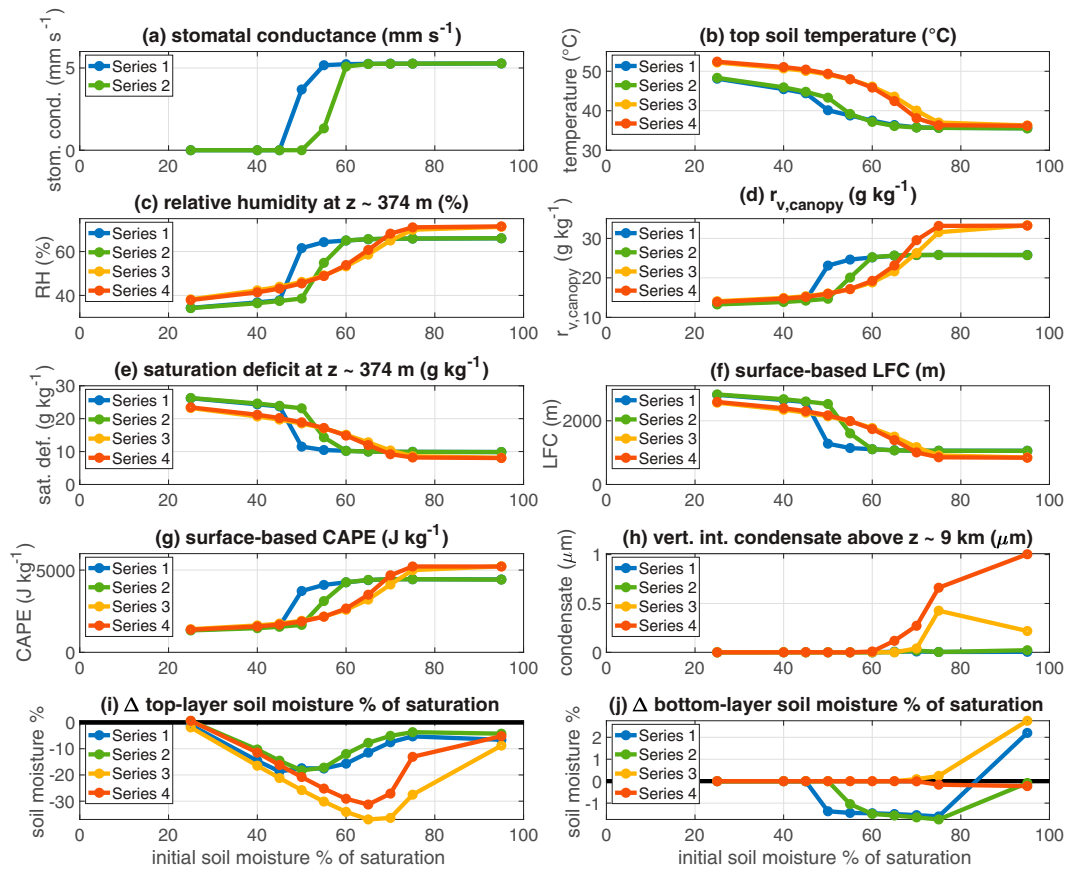


FIG. 5. Quantities for all four series of simulations as a function of initial soil moisture, averaged over 1200–1800 LT: (a) horizontal-mean stomatal conductance for vegetated simulations (Series 1 and Series 2); (b) horizontal-mean temperature of the uppermost soil layer; (c) horizontal-mean relative humidity at  $z \sim 374$  m; (d) canopy water vapor mixing ratio; (e) horizontal-mean saturation deficit at  $z \sim 374$  m; (f) surface-based LFC of the domain-mean sounding; (g) surface-based CAPE of the domain-mean sounding; (h) horizontal-mean liquid-equivalent vertically integrated condensate above  $z \sim 9$  km; (i) difference between the 1200–1800 LT mean top-layer (top 1 cm) soil moisture and the initialization value; and (j) as in (i), but for the bottom soil layer (located 40–50 cm below the surface). The LFC and CAPE are calculated using the procedure outlined in appendix A.

wet-soil simulations appears to be the PWP, which occurs between 45% and 50% of saturation for the silty clay loam soil type used in Series 1. This partitioning is to be expected given the response of stomatal conductance to soil moisture in Fig. 4a. The root-zone soil moisture depletion over the course of the day is limited to a few percentage points of saturation (Fig. 5j) and therefore affects transpiration only minimally.

Surface evaporation does play a role in determining the total latent heat flux (Fig. 6i), which exceeds transpiration by up to  $\sim 200\text{--}300 \text{ W m}^{-2}$  (not shown). There is more variation in latent heat fluxes within each of the two groups than can be explained by the variation in stomatal conductance alone. We therefore conclude that the within-group variation in latent heat flux is due to differences in surface evaporation. In particular, the latent heat flux is larger as initial soil moisture is increased from 50% (just above the PWP) to 65% (just below the field capacity). Within simulations initialized with soil wetter than the field capacity (S1M70, S1M75, and S1M95), there

is minimal gain in latent heat flux with additional increases in the initial soil moisture. The overall trend in latent heat flux with increasing initial soil moisture, therefore, reflects a superposition of the soil moisture–stomatal conductance relationship seen in Fig. 4a and the soil moisture–surface evaporation relationship seen in Fig. 4b. The actual domain-mean  $r_{v,\text{canopy}}$  is shown in Fig. 5d in order to enable comparison with Fig. 4b, which illustrates the soil moisture–surface evaporation relationship for just one specified value of  $r_{v,\text{canopy}}$ . The top-layer soil moisture, which controls direct surface evaporation, does evolve substantially over the course of the day in some cases (Fig. 5i). For example, it drops by about 20 percentage points of saturation in S1M50. However, it drops only by a few percentage points of saturation in S1M75 and S1M95. This evolution amplifies the impacts of the soil moisture–surface evaporation relationship on the total surface latent heat fluxes.

Figure 6 shows the individual terms of the surface energy budget, with ground heat flux (Fig. 6g) defined positive

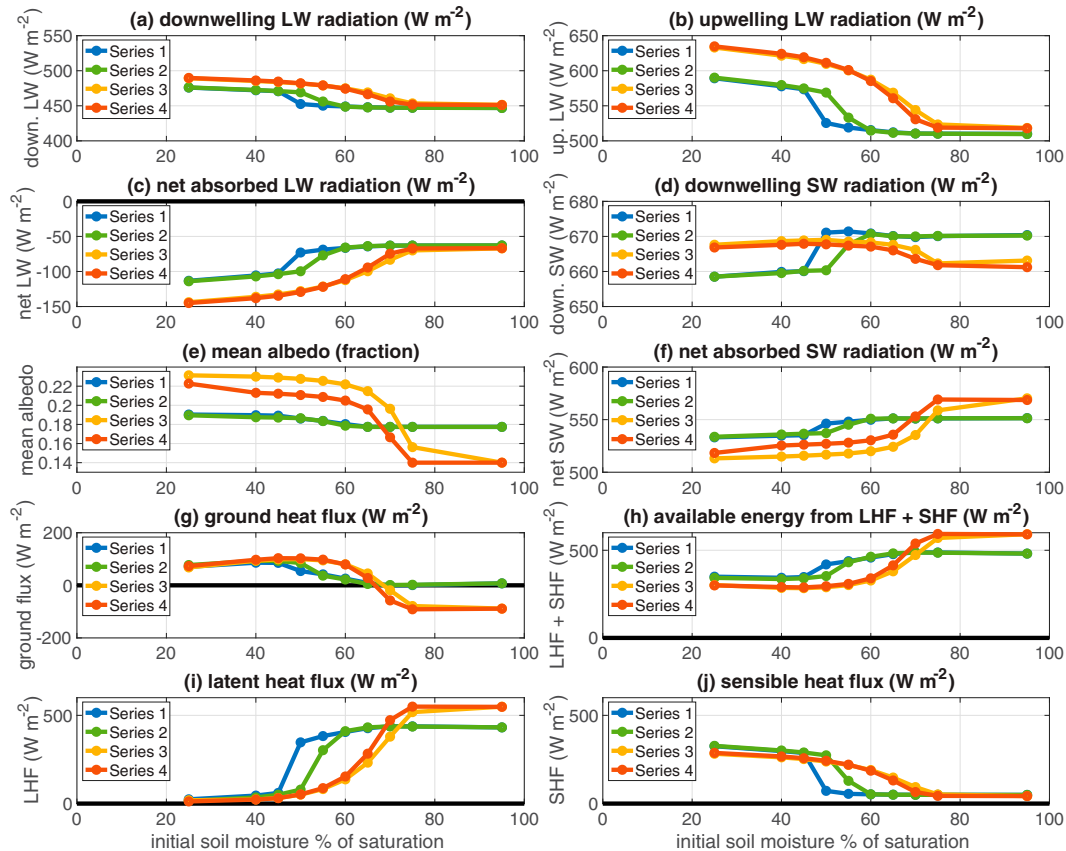


FIG. 6. Surface energy budget for all four series of simulations as a function of initial soil moisture, averaged over 1200–1800 LT: (a) downwelling longwave radiation reaching the surface; (b) upwelling longwave radiation from the surface; (c) net absorbed longwave radiation at the surface [(a) minus (b)]; (d) downwelling shortwave radiation reaching the surface (note relatively small range of values); (e) mean surface albedo with respect to shortwave radiation; (f) surface absorbed shortwave radiation based on values in (d) and (e); (g) ground heat flux, calculated as a residual under the assumption of balance between the energy budget terms; (h) the available energy, defined as the sum of surface latent and sensible heat fluxes; (i) surface latent heat flux; and (j) surface sensible heat flux.

downward and latent and sensible heat fluxes (Figs. 6i and j, respectively) defined positive upward. Of particular interest for the atmospheric response to changes in soil moisture is the partitioning of the available energy (Fig. 6h) into latent heat fluxes and sensible heat fluxes. The available energy is constrained by the radiative fluxes (see Figs. 6a–f) and ground heat fluxes. In Series 1, there is more available energy for wet-soil simulations than for dry-soil simulations. Upwelling longwave radiation (Fig. 6b) decreases with increasing soil moisture, resulting in  $\sim 50 \text{ W m}^{-2}$  less net emission of longwave radiation into the atmosphere (Fig. 6c). There is also  $\sim 100 \text{ W m}^{-2}$  less loss of thermal energy into the ground (Fig. 6g). There are also slight changes in downwelling shortwave radiation (Fig. 6d) and albedo (Fig. 6e). Despite the overall increase in available energy with increasing soil moisture, the partitioning of the available energy also changes, with a substantial decrease in sensible heat flux with increasing soil moisture. As was observed for latent heat fluxes, the Series 1 simulations are

partitioned into two groups with respect to sensible heat fluxes (Fig. 6j): three simulations initialized with soil drier than the PWP, and seven simulations initialized with soil wetter than the PWP.

## 2) WETTER-SOIL SIMULATIONS HAVE LOWER LFCs

The seven wettest-soil simulations exhibit much larger surface latent heat fluxes (Fig. 6i) and much smaller surface sensible heat fluxes (Fig. 6j) than do the three driest-soil simulations. Therefore, the near-surface temperatures are cooler and the near-surface water vapor mixing ratios are greater. These, in turn, lower the lifted condensation level (LCL) and the level of free convection (LFC, Fig. 5f), enabling near-surface-based parcels to reach their LFCs without undergoing as much ascent as would otherwise be required. Among the seven wettest-soil simulations, the driest of these, S1M50, exhibits the highest LFC ( $\sim 1280 \text{ m}$ ), and the wettest, S1M95, exhibits the lowest LFC ( $\sim 1060 \text{ m}$ ; Fig. 5f).

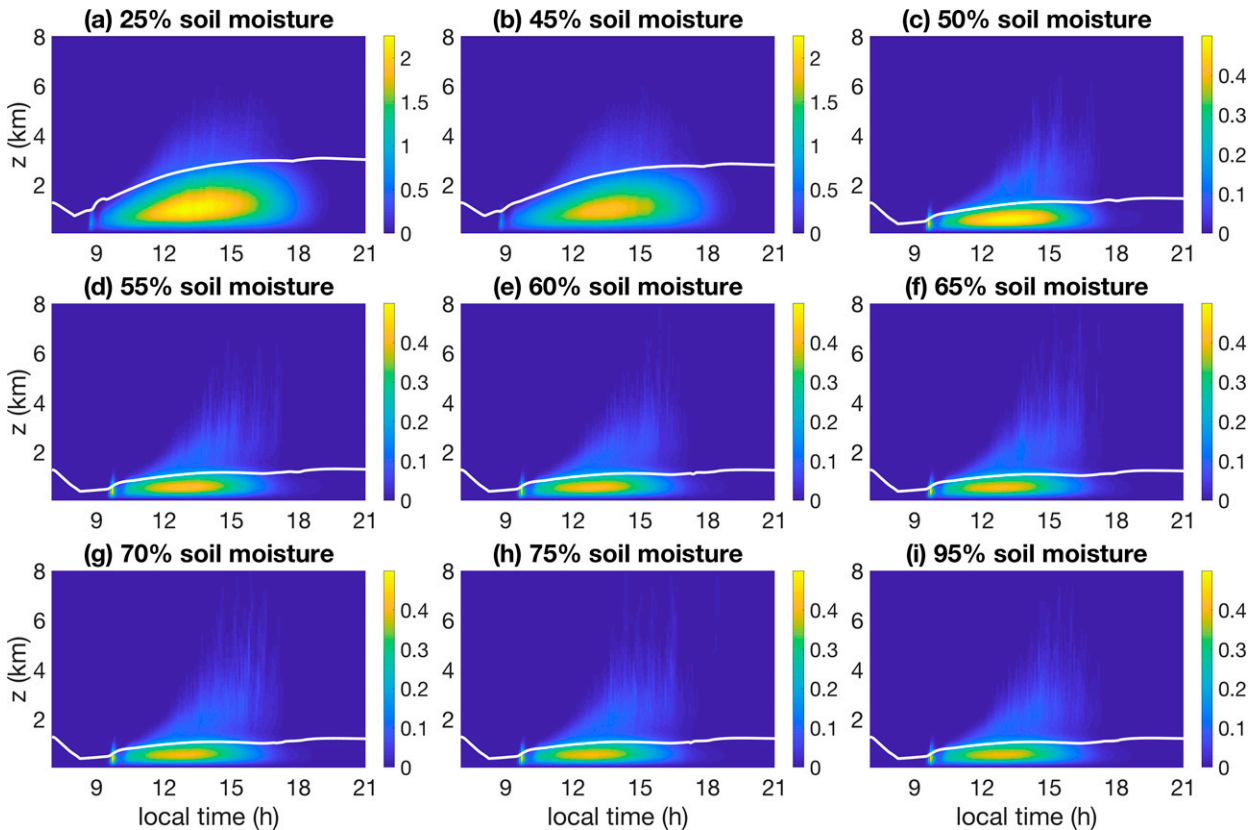


FIG. 7. Domain-mean kinetic energy of vertical motions ( $\text{J kg}^{-1}$ ), computed by taking the horizontal average of  $w^2/2$  (where  $w$  is the vertical velocity), is plotted in the color shading as a function of time and altitude for 9 out of the 10 simulations in Series 1 (wooded grassland, silty clay loam). The surface-parcel-based LFC, based on the domain-mean sounding at each output time, is plotted in white. S1M40 is omitted here and in Fig. 8 due to graphical constraints but behaves qualitatively similarly to S1M25 and S1M45. Note that the first two panels use a different color scale than do the remaining seven.

3) BOUNDARY LAYER VERTICAL MOTIONS ARE STRONGER UNDER DRY-SOIL CONDITIONS

We now discuss the implications of changes in sensible and latent heat fluxes across Series 1. As soil moisture decreases, stronger sensible heat fluxes drive stronger boundary layer vertical motions (Fig. 7). The three driest-soil simulations exhibit much stronger boundary layer vertical motions than do the seven wettest-soil simulations, to the extent that different color scales must be used for the two groups in order to be able to discern the within-group trends. The three driest-soil simulations also exhibit the deepest boundary layer circulations.

4) STRONGER VERTICAL MOTIONS LEAD TO ENHANCED CLOUDINESS AND PRECIPITATION PRODUCTION IN DRIEST-SOIL SIMULATIONS

These boundary layer motions, in turn, generate clouds near the top of the boundary layer. Cloud fraction values (Fig. 8) are greater, and clouds are deeper, in the three driest-soil simulations than in the seven wettest-soil simulations. A possible mechanism for the increased cloudiness is the scaling of convective plume width with subcloud layer depth, such

that clouds forming above deeper subcloud layers are wider (Williams and Stanfill 2002; Lucas et al. 1994). Another possible mechanism is enhanced overshooting of the LCL by vigorous convective plumes in the three driest-soil simulations, which would result in deeper clouds regardless of whether the LFC is reached. The increased cloudiness in the three driest-soil simulations translates into enhanced precipitation formation (Fig. 9a; broken dark blue curve).

5) MORE ENTRAINMENT FOR RISING PARCELS IN S1M50 THAN IN WETTER-SOIL SIMULATIONS

Within the same group of seven simulations as discussed previously, boundary layer relative humidity is lowest in S1M50 [within the lowest  $\sim 1.3$  km of the atmosphere, and lower than the S1M95 value by as much as  $\sim 7.5$  percentage points (at a vertical level other than that shown in Fig. 5c; not shown)]. As a result, not only do S1M50 parcels need to ascend further (than in S1M95) in order to reach their LFC, but they also entrain drier air as they rise, thereby reducing their ability to reach their LFC. The amount of entrainment may be greater in S1M50 as well, given that this simulation exhibits slightly stronger boundary layer motions in general than do

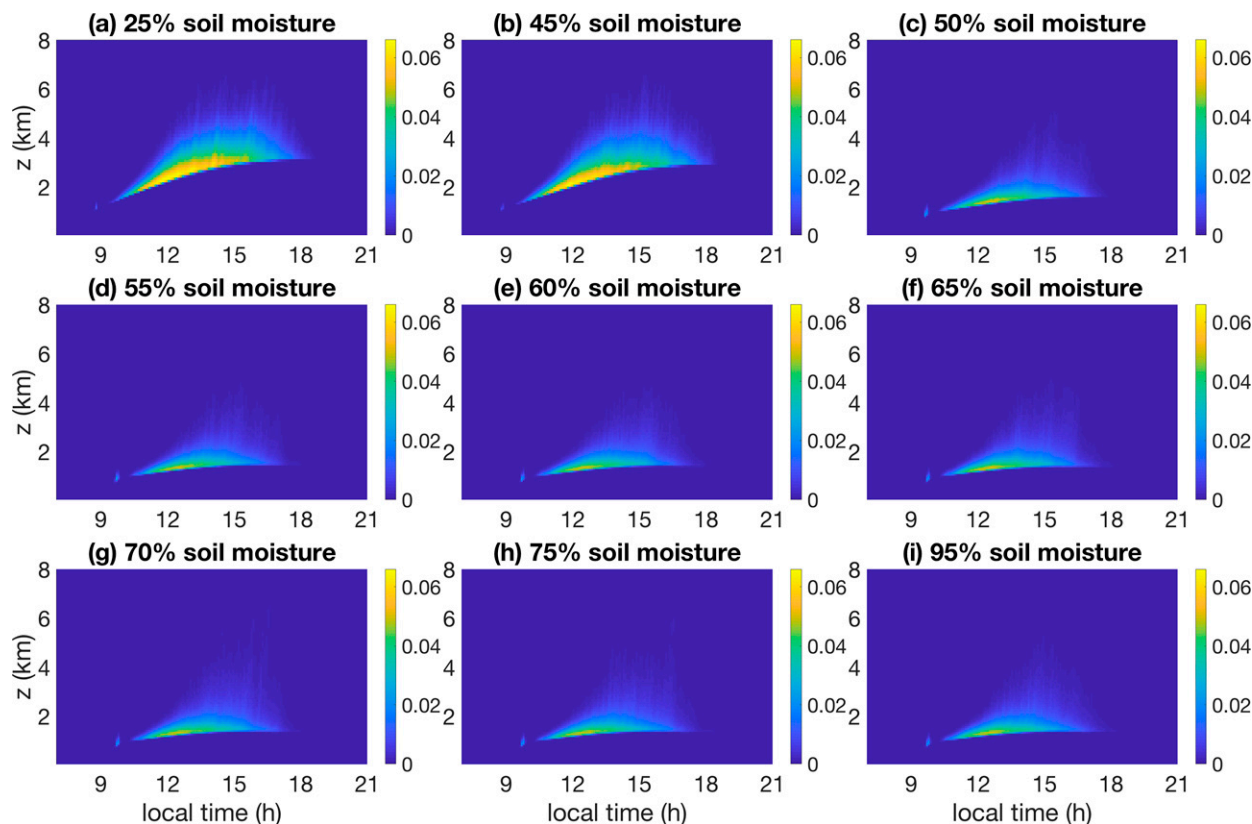


FIG. 8. Cloud fraction, calculated as the fraction of points at a given height with a total cloud water and cloud ice mixing ratio of at least  $0.1 \text{ g kg}^{-1}$ , as a function of time and altitude for nine out of the ten simulations in Series 1 (wooded grassland, silty clay loam).

the progressively wetter-soil simulations (Fig. 7). Although the effects of increased LFC height may be counteracted somewhat by the increased strength of boundary layer updrafts in S1M50, the latter evidently does not dominate, as less precipitation ultimately forms in S1M50 than in the wetter-soil simulations (Fig. 9a; broken dark blue curve).

#### 6) EVAPORATION OF FALLING PRECIPITATION

Not all of the rain that is produced by these clouds reaches the ground. Less than half of the precipitation that forms aloft reaches the ground, with especially low values in the three driest-soil simulations (Fig. 9a; black curve). Several factors influence the proportion of rain reaching the ground, including the subcloud layer's depth, dryness, and turbulence.

The subcloud-layer saturation deficit, i.e., the difference between the saturation water vapor mixing ratio and the actual water vapor mixing ratio, varies tremendously across simulations (Fig. 5e displays values for a single subcloud vertical level). The saturation deficit is larger in the three driest-soil simulations than in the seven wettest-soil simulations. Furthermore, the subcloud layer is deeper in the three driest-soil simulations (Fig. 8). Therefore, falling rain drops have both more time to evaporate and greater instantaneous evaporation rates (which depend upon saturation deficit) in the three driest-soil simulations. Since the subcloud layer in these

simulations is also generally more turbulent (Fig. 7), there may also be more entrainment of dry air into rain shafts. As a result, the fraction of rain that reaches the surface is much lower in the three driest-soil simulations than in the seven wettest-soil simulations. Among the seven wettest-soil simulations, there is a greater (by  $\sim 2.5 \text{ g kg}^{-1}$ ) subcloud-layer saturation deficit in S1M50 than in S1M95. Due to these subcloud layer properties, a greater fraction of rain evaporates before reaching the surface in S1M50 than in the wettest-soil simulations (Fig. 9a; magenta curve). Partitioning of the evaporation budget between levels below and above cloud base confirms that this is due to greater evaporation in the subcloud layer (Fig. 9a; cyan and yellow curves). Therefore, the intermediate-soil-moisture disadvantage in surface accumulation (reproduced in the solid dark blue curve in Fig. 9a) is produced by a combination of diminished rain production aloft and enhanced subcloud-layer evaporation of the rain that is produced.

#### 7) TIMING OF PRECIPITATION ONSET

We now discuss the mechanisms behind the differences in precipitation onset time across the simulations in Series 1. As discussed previously, the onset of surface rainfall is earlier in the three dry-soil simulations (S1M25, S1M40, and S1M45) and later in the seven wet-soil simulations. However, among the seven wet-soil simulations, the four wettest-soil simulations

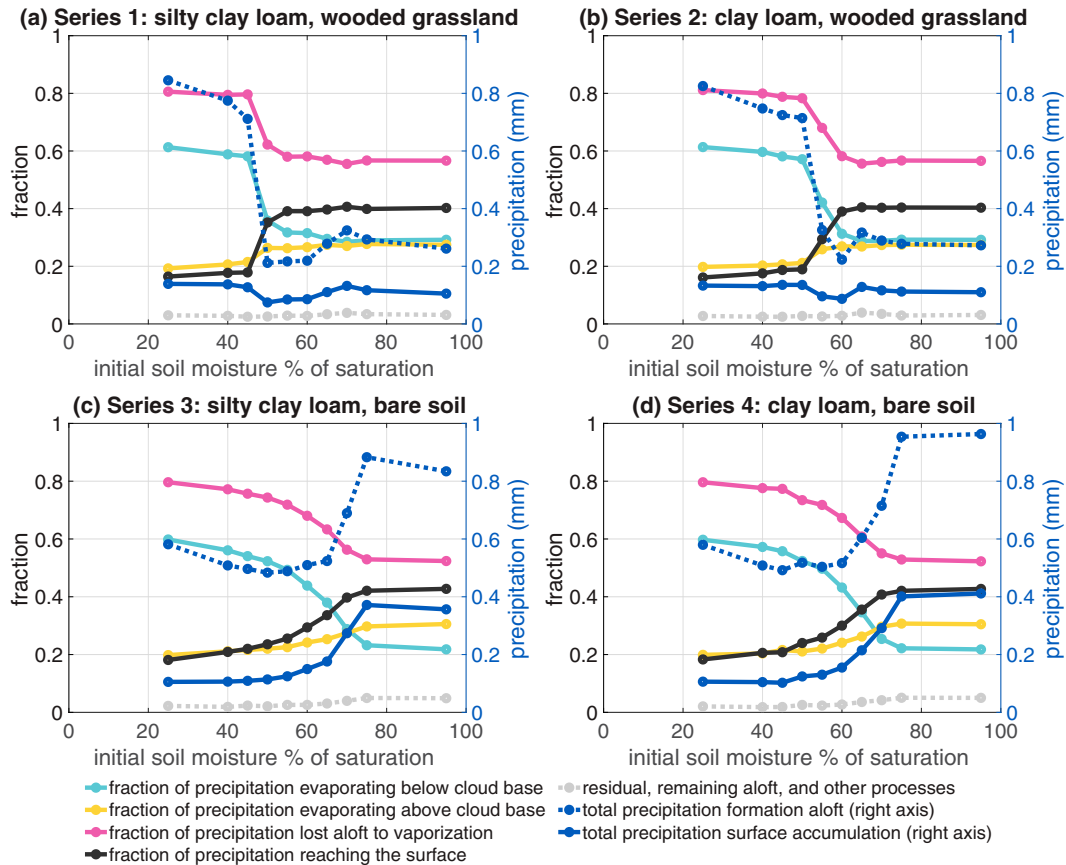


FIG. 9. Spatially (entire domain) and temporally (entire simulation duration) integrated precipitation budgets for all four series of simulations. The four panels correspond to the four series of simulations, as labeled. The line colors follow the legend at the bottom of the figure. The first five quantities are plotted using the left vertical axis, and the final two are plotted using the right vertical axis. Quantities on the left vertical axis are expressed as fractions of total precipitation formation aloft, which itself is plotted on the right vertical axis. Total precipitation formation aloft is defined as the sum of collision–coalescence of cloud droplets into rain drops and conversion of cloud mass to snow, aggregates, graupel, and hail mass via riming. Cloud base is defined hourly within each simulation (see appendix C). The cyan and yellow curves sum exactly to the magenta curve. The magenta and black curves sum approximately to 1, with the deviation from 1 plotted in the broken light gray curve. The solid dark blue curve in each panel is reproduced here from Fig. 2.

(S1M65, S1M70, S1M75, and S1M95) exhibit an earlier onset of surface rainfall than do the three drier-soil simulations within the group (S1M50, S1M55, and S1M60). In order for precipitation to form in any given environment, lower boundary layer–based parcels must ascend beyond their LFCs, which are virtually identical to their LCLs in these simulations.

The white curves in Fig. 7 indicate the LFC time evolution for each simulation. The dry-soil simulations (S1M25, S1M40, and S1M45) experience the earliest precipitation because there is more surface sensible heating. This sensible heating causes more rapid boundary layer development and thus stronger boundary layer vertical motions. These motions enable parcels to reach their LFCs, despite the fact that the LFCs are elevated relative to those in the seven wet-soil simulations. Even though the boundary layer motions reach their maximum magnitudes around the same time in each of the

simulations, these motions are much weaker overall in the wet-soil simulations than in the dry-soil simulations.

Several possible mechanisms could be responsible for the delay in precipitation onset within the intermediate-soil-moisture simulations (S1M50, S1M55, and S1M60) relative to the four wettest-soil simulations. The intermediate-soil-moisture simulations, by virtue of their enhanced surface sensible heat fluxes (Fig. 6j), exhibit slightly deeper and stronger boundary layer circulations than do the wettest-soil simulations (Fig. 7; compare the brightest yellow in Fig. 7c to that in Figs. 7d–i). Moreover, they exhibit drier subcloud layers (Fig. 5e). As a result, entrainment of dry ambient air into rising convective plumes, which acts to suppress rain formation, can be expected to be enhanced in the intermediate-soil-moisture simulations. Furthermore, rain shafts in the intermediate-soil-moisture simulations may be expected to encounter and entrain more dry air, resulting in more evaporation of falling precipitation within the

subcloud layer. Both of these factors may result in the delayed onset of precipitation in the intermediate-soil-moisture simulations relative to the wettest-soil simulations.

*d. Series 1 versus Series 2 (vegetated): Role of the permanent wilting point*

The trends in Series 2 largely mirror those in Series 1, although there are some important differences. Recall that the silty clay loam soil type (Series 1) has a PWP between 45% and 50% of saturation, whereas clay loam (Series 2) has a PWP between 50% and 55% of saturation. Therefore, while S1M50 is initialized with soil that is moister than the PWP, S2M50 is initialized with soil that is drier than the PWP.

It was shown previously that the PWP governs stomatal conductance and thus much of the surface flux partitioning, and it was speculated previously that this PWP threshold is responsible for the fact that various aspects of the Series 1 simulations readily organize into two groups of simulations with similar within-group properties: a group of three dry-soil simulations and a group of seven wet-soil simulations. Figures 5a–g reveal that the transition from dry-soil behavior to wet-soil behavior of several domain-mean quantities occurs at greater soil moisture values in Series 2 than in Series 1: the green curves are shifted to the right of the blue curves by 5–10 initial soil moisture fraction percentage points, in accordance with the ~7-percentage-point difference in PWP values. A similar comparison can be obtained via careful examination of Figs. 9a,b. These results provide evidence that it is indeed the PWP threshold that divides the two groups.

*e. Summary of mechanisms leading to the nonmonotonic soil moisture–precipitation relationship*

The nonmonotonic soil moisture–precipitation relationship consists of a piecewise dry-soil advantage for dry soils, a piecewise wet-soil advantage for wet soils, and consequently a minimum in precipitation amount for intermediate soil moistures. It results from an interplay between soil moisture, vegetation, boundary layer properties, and cloud properties. In order for rain to form, rising plumes must reach the LFC. In order for rain to reach the surface and accumulate, it must not evaporate aloft. For dry soils, decreasing soil moisture results in increased surface sensible heating and therefore more vigorous convective plumes that can reach elevated LFCs. For wet soils, increasing soil moisture results in moister convective plumes that are less susceptible to entrainment of dry air and need not rise as far as in the dry-soil case in order to reach the LFC. Intermediate-wetness soils barely above the PWP threshold generate precipitation through a mechanism similar to that of the wettest soils, but they do so less efficiently: the modestly drier and more turbulent subcloud layers substantially inhibit both the formation of precipitation aloft and raindrops' survival as they fall toward the surface.

*f. Without vegetation*

In the absence of vegetation (Series 3 and Series 4), there is no transpiration, and so latent heat fluxes are governed entirely by surface evaporation. Therefore, the PWP threshold,

which does not enter the calculation of surface evaporation, does not play a direct role. Recall that the transition in surface evaporation from dry soil to wet soil is much more gradual (Fig. 4b) than in transpiration (Fig. 4a). As a result, each nonvegetated series of simulations exhibits a smooth transition from dry soil to wet soil, rather than an abrupt transition at the PWP that partitions the series into two groups as is seen in the vegetated simulations.

Given surface evaporation's dependence on field capacity (~68% for both soil types tested; Fig. 4b), surface evaporation might initially be expected to be a very weak function of initial soil moisture for values at and above 70%. However, as was the case with Series 1, the soil moisture at the top soil level decreases substantially over the course of the day in some of the simulations (Fig. 5i), and as a result, Series 3 and Series 4 each exhibit nonidentical behavior among the three wettest-soil simulations in the respective series.

Overall, in Series 3 and Series 4 (nonvegetated), more rain generally reaches the surface under wet-soil conditions than under dry-soil conditions (Fig. 2). This result contrasts with the results from Series 1 and Series 2 (vegetated), for which the most rain reaches the surface under dry-soil conditions and the least rain reaches the surface for soils slightly moister than the PWP. Furthermore, for the wet-soil simulations, nearly 300% more rain reaches the surface in the nonvegetated simulations than in the vegetated simulations.

Different processes dominate when vegetation is present than when vegetation is absent. Most obviously, there is no transpiration; all latent heat fluxes take the form of direct surface evaporation. It appears that several factors are responsible for the trends in the nonvegetated simulations. The first is that the latent heat fluxes in the nonvegetated wet-soil simulations are enhanced compared to the vegetated wet-soil simulations (Fig. 6i). For the S60, S65, and S70 simulations, this is especially true during the morning hours (not shown). This latent heat flux enhancement may be related to greater top soil layer heating due to the lack of shading by vegetation (Fig. 5b). As compared to the nonvegetated dry-soil simulations, the nonvegetated wet-soil simulations also exhibit ~100% more available energy for total latent and sensible heat fluxes (Fig. 6h) due to changes in ground heat flux (Fig. 6g), decreased albedo for wet soils (Fig. 6e) and decreased net loss of longwave radiation (Fig. 6c) for the cooler wet soils (Fig. 5b). This large increase in available energy (particularly in the form of latent heat fluxes) enables the development of large amounts ( $>5000 \text{ J kg}^{-1}$ ) of convective available potential energy (CAPE, Fig. 5g) and very low LFCs (~800 m; Fig. 5f). Deep convection is therefore able to emerge in the wettest-soil, nonvegetated simulations (Fig. 5h), resulting in enhanced rainfall.

Even when deep convection does not emerge, such as in S3M60/S4M60, there is an increase in rainfall relative to S1M60/S2M60, and this occurs despite decreased CAPE and a higher LFC. We speculate that this is due to the timing of the sensible and latent heat fluxes in the absence of vegetation. When vegetation is absent, all latent heat fluxes are supplied by the uppermost soil level since there are no roots to access the lower soil levels. Furthermore, due to changes in hydraulic conductivity of the soil, the moisture in the

uppermost soil level becomes more difficult to replenish from below as the soil dries. Therefore, in simulations such as S3M60/S4M60, latent heat fluxes give way to sensible heat fluxes over the course of the early afternoon when vegetation is absent. This combination of morning moistening and afternoon sensible heating results in an atmosphere that more readily produces surface precipitation. The last factor responsible for the trends in the nonvegetated simulations is that, as was found for the vegetated simulations, a greater fraction of the rain that is produced reaches the surface in wet-soil simulations than in dry-soil simulations due to the presence of a moister subcloud layer and therefore less subcloud evaporation of rain (Figs. 9c,d).

#### 4. Discussion and conclusions

In this study we have presented a nonmonotonic soil moisture–precipitation relationship in which soils initialized slightly moister than the PWP (intermediate soil moistures) receive less rain than do very wet or very dry (sub-PWP) soils. Under this regime, intermediate-wetness soils also experience the latest onset of precipitation. This *intermediate disadvantage* occurs only when vegetation is present, as it is largely the vegetation, via transpiration, that makes the PWP relevant.

Under the vegetated conditions tested in the Series 1 and Series 2 simulations, the strong sensible heat fluxes induced by dry soils promote strong boundary layer vertical motions that are able to reach and exceed the LFC, which spurs condensation and the formation of precipitation. However, much of the precipitation evaporates before reaching the land surface due to the dryness of the boundary layer. On the other hand, when soil is wet, latent heat fluxes result in moistening of the near-surface layer and therefore act to lower the LFC. This lowering of the LFC enables the relatively weak boundary layer motions to reach the LFC more easily.

In vegetated intermediate-soil-moisture simulations, initialized with soil slightly wetter than the PWP, the sensible heat fluxes are slightly stronger than in the wettest-soil simulations, and the latent heat fluxes are slightly weaker. These changes act to strengthen the boundary layer motions and increase the LFC relative to the wettest-soil simulations. Evidently, in terms of precipitation, the slightly increased boundary layer motion strength is insufficient to offset the effects of an increased LFC. The boundary layer as a whole becomes drier than in the wettest-soil simulations, which acts both to decrease the relative humidity within updrafts and to promote subcloud evaporation of falling precipitation. As a result, the intermediate-soil-moisture simulations receive approximately two-thirds as much surface precipitation as do the wettest-soil and driest-soil simulations.

The present study implies the possibility that *wet-soil advantage* and *dry-soil advantage* are, at times, neither complete nor mutually exclusive descriptors. They are incomplete in that neither fully describes the response of afternoon precipitation to soil moisture. And although they seemingly describe opposite regimes, both responses are present in a “piecewise” sense in the soil moisture–precipitation relationship obtained

here. In Series 1 and 2, precipitation decreases with increasing soil moisture as the initial soil moisture approaches the PWP, constituting a dry-soil advantage. Then, as initial soil moisture increases toward the field capacity, the precipitation increases with increasing soil moisture, which constitutes a wet-soil advantage. In other words, dry soils exhibit a dry-soil advantage, and wet soils exhibit a wet-soil advantage for the same initial atmospheric conditions. The potential existence of nonmonotonic responses, as suggested by the present study, is not considered by theoretical frameworks such as that of Findell and Eltahir (2003b).

The nonvegetated Series 3 and Series 4 do not experience the nonmonotonic soil moisture–precipitation response that constitutes the main focus of this study. Instead, there is a wet-soil advantage. The precipitation trends with changes in soil moisture do not exhibit strong PWP dependence either; instead, there is a gradual transition in simulation properties with changes in soil moisture. These results are attributable to the nondependence of direct surface evaporation of moisture on the PWP in the LEAF-3 scheme.

It is worth noting that when only the extreme cases (M25 and M95) of Series 1 and Series 2 (both vegetated) are considered, the CTP-HI<sub>low</sub> framework of Findell and Eltahir (2003b) does perform as intended. The CTP-HI<sub>low</sub> framework predicts that our initial sounding will give rise to a dry-soil advantage situation, and indeed, the driest-soil simulations exhibit earlier onset and somewhat greater rainfall accumulation than do the wettest-soil simulations. However, the CTP-HI<sub>low</sub> framework does not predict the wet-soil advantage obtained in the bare-soil simulations (Series 3 and Series 4). The existence of opposite soil moisture–precipitation relationships over vegetated surfaces compared with bare soils suggests that different mechanisms may be active during different parts of the growing season as vegetation properties change.

Now that the present study has uncovered the possibility of a strongly nonmonotonic soil moisture–precipitation response, future work should assess the conditions under which such a response is likely to occur, as well as the relevance of this response to the broader climate and water supply challenges that motivated this work. In particular, the sensitivity of this response to the environmental setup and model parameterizations should be probed, as we will now discuss:

- 1) The environmental setup:
  - (i) In using a single initial sounding (Fig. 1) to initialize all simulations, we have sampled only one point in CTP-HI<sub>low</sub> space, and it is likely that other initial soundings, particularly those with different wind profiles (Findell and Eltahir 2003a; Cioni and Hohengerger 2017) and CTP-HI<sub>low</sub> classifications, would produce different responses. Given the overall low domain-mean rainfall totals in our simulations, it is especially important to examine whether the nonmonotonic soil moisture–precipitation response can be reproduced in simulations whose initial thermodynamic, moisture, and wind profiles correspond to observed events that produced greater precipitation totals.

- (ii) We designed our simulations to emulate conditions at a single geographical location (Luzon in the Philippines) at a single time of year (early August), and our simulations lacked coastlines, topography, and Coriolis deflection. These, as well as seasonal differences in vegetation albedo and insolation, all represent elements that may be adjusted in future studies. Additional soil textures and vegetation types also ought to be examined.
  - (iii) We have only considered short-duration simulations with essentially horizontally homogeneous initial conditions. Although such simulations are essential for elucidating processes, there exist other soil moisture–precipitation mechanisms in nature that emerge only in the presence of heterogeneity (e.g., Schneider et al. 2019; Taylor et al. 2012) or over the course of several days (Schlemmer et al. 2012).
- 2) Model parameterizations:
- (i) Other models use different formulations of direct surface evaporation. For instance, the scheme of Chen and Dudhia (2001) eliminates surface evaporation below the PWP and therefore might produce results that vary from ours. The specific formulation of bare-soil evaporation represents a source of uncertainty meriting further investigation.
  - (ii) Our results for Series 1 and Series 2 (vegetated) may be sensitive to the step-like behavior of the stomatal conductance formulation (with respect to soil moisture) used in LEAF-3. Figure 9 of Powell et al. (2013), which corresponds to our Fig. 4a, summarizes several other land surface models' formulations. Their behavior ranges from step-like, as in Community Land Model version 3.5 (Oleson et al. 2008), to gradual, as in the Joint U.K. Land Environment Simulator version 2.1 (Cox et al. 1999; Clark et al. 2011). Clearly, there is substantial uncertainty in the stomatal response to soil moisture–related water stress. This uncertainty may be compounded by different responses for different plant species (e.g., section A.6.4 of White et al. 2000). An intercomparison involving models with different vegetation parameterizations would be useful for assessing the sensitivity of our nonmonotonic precipitation response to the transpiration formulation. Further experiments using RAMS/LEAF-3 that adjust the shape of the stomatal conductance curve in Fig. 4a may also yield helpful insights.

Each of these areas for future research may further our understanding of the conditions under which a nonmonotonic response with an intermediate-soil-moisture disadvantage may be likely to occur. Such research may also illuminate how vegetation–cloud–precipitation relationships may behave in changing climates. It is also essential to assess the response's occurrence in observations and to expand existing theory to account for the existence of nonmonotonic soil moisture–precipitation relationships.

*Acknowledgments.* This work was funded by the Office of Naval Research under Grant N00014-16-1-3093, and simulations

were performed on the Navy Department of Defense Supercomputing Resource Center Cray XC40 system *Conrad*. We acknowledge useful discussions with Prof. Elizabeth A. Barnes regarding the calculation of the confidence intervals in Fig. 2. Dr. Kirsten L. Findell directed us to some helpful resources during the initial stages of this work. We also acknowledge the valuable perspectives and insights into soil science that Emily M. Lacroix provided while the manuscript was in revision. Finally, we gratefully acknowledge Dr. Christopher Taylor and two anonymous reviewers, whose insightful comments have resulted in an improved manuscript.

*Data availability statement.* The raw and processed RAMS model outputs produced as part of this study are too large to store and transfer. However, our plotting code, the summary data necessary to reproduce the plots, and all model and analysis code necessary to reproduce our full results from scratch (save for any machine and compiler sensitivity), are all available at the Mountain Scholar repository (<http://dx.doi.org/10.25675/10217/235131>).

## APPENDIX A

### Calculating Parcel Theory Indices

Calculations of variables derived from parcel theory, such as CAPE and the LFC, are performed using a version of the `getcape.F` code (version 1.04) from Cloud Model 1 (Bryan and Fritsch 2002) that has been modified to use the physical constants and thermodynamic formulas used in RAMS. All calculations are pseudoadiabatic, and the latent heat of freezing is not considered.

## APPENDIX B

### Calculating Error Bars in Fig. 2

To assess statistical significance of trends in total accumulated precipitation, we partition the 100 km × 100 km domain into a 5 × 5 grid of 20 km × 20 km subdomains. The mean precipitation is calculated for each of the 25 subdomains, and 95% confidence intervals for the mean are constructed using bootstrapping. Implicit in this process is the assumption that the subdomains are statistically independent of one another, which appears to be approximately true given the small cloud sizes. In increasing the number of subdomains to values as large as 400, we find that the confidence interval bounds exhibit minimal sensitivity to the number of subdomains.

## APPENDIX C

### Full Explanation of Fig. 9 Calculations

Mixing ratios are output by the model every 5 min, whereas process rates are output on an hourly basis based on accumulated totals over the previous hour. Therefore, we define a unique cloud base height on an hourly basis (for computing the hourly precipitation formation and evaporation rates) using

the 5-min-output cloud liquid and pristine ice (cloud ice) mixing ratios from the previous hour.

For example, the 1400 LT value of cloud base is calculated as follows: Take the horizontal-mean cloud mass per unit volume (mixing ratio multiplied by the model base-state density) at each 5-min output time from 1300 to 1400 LT. Take a weighted average of these 13 values, giving the middle 11 values a double weight (i.e., trapezoidal integration). We look backward through the previous hour because the hourly budget variables were accumulated through the previous hour. Take  $d/dz$  of the result (centered-in-space finite differences at “half-levels” in between the model levels at which the rates and mixing ratios are defined), and look for where this is maximized. Assuming this is maximized and positive at some location, this half-level is designated as cloud base. The model levels below cloud base count as subcloud, and the model levels above cloud base count as within/above cloud. A time-varying cutoff, unique for each simulation, results.

Spatial and temporal integration is performed next. This process results in a single value for each simulation for the total precipitation formation aloft, total precipitation condensation/evaporation below cloud base, and total precipitation condensation/evaporation above cloud base. The total precipitation lost aloft to vaporization is the exact sum of the below- and above-cloud-base values. The fractional values are obtained by multiplying by  $-1$  (such that net evaporation becomes positive) and then dividing by the total precipitation formation aloft. The fraction of precipitation reaching the surface is obtained by calculating the spatially and temporally integrated accumulated precipitation (output by the model) and dividing by the total precipitation formation aloft. The residual is then obtained as  $1 -$  (fraction of precipitation lost to vaporization)  $-$  (fraction of precipitation reaching the surface).

## REFERENCES

- Baranowski, D. B., D. E. Waliser, X. Jiang, J. A. Ridout, and M. K. Flatau, 2018: Contemporary GCM fidelity in representing the diurnal cycle of precipitation over the Maritime Continent. *J. Geophys. Res. Atmos.*, **124**, 747–769, <https://doi.org/10.1029/2018JD029474>.
- Berg, A., and J. Sheffield, 2019: Evapotranspiration partitioning in CMIP5 models: Uncertainties and future projections. *J. Climate*, **32**, 2653–2671, <https://doi.org/10.1175/JCLI-D-18-0583.1>.
- Bryan, G. H., and J. M. Fritsch, 2002: A benchmark simulation for moist nonhydrostatic numerical models. *Mon. Wea. Rev.*, **130**, 2917–2928, [https://doi.org/10.1175/1520-0493\(2002\)130<2917:ABSFMN>2.0.CO;2](https://doi.org/10.1175/1520-0493(2002)130<2917:ABSFMN>2.0.CO;2).
- , J. C. Wyngaard, and J. M. Fritsch, 2003: Resolution requirements for the simulation of deep moist convection. *Mon. Wea. Rev.*, **131**, 2394–2416, [https://doi.org/10.1175/1520-0493\(2003\)131<2394:RRFTSO>2.0.CO;2](https://doi.org/10.1175/1520-0493(2003)131<2394:RRFTSO>2.0.CO;2).
- Chen, F., and J. Dudhia, 2001: Coupling an advanced land surface–hydrology model with the Penn State–NCAR MM5 modeling system. Part I: Model implementation and sensitivity. *Mon. Wea. Rev.*, **129**, 569–585, [https://doi.org/10.1175/1520-0493\(2001\)129<0569:CAALSH>2.0.CO;2](https://doi.org/10.1175/1520-0493(2001)129<0569:CAALSH>2.0.CO;2).
- Cheng, W. Y. Y., and W. R. Cotton, 2004: Sensitivity of a cloud-resolving simulation of the genesis of a mesoscale convective system to horizontal heterogeneities in soil moisture initialization. *J. Hydrometeorol.*, **5**, 934–958, [https://doi.org/10.1175/1525-7541\(2004\)005<0934:SOACSO>2.0.CO;2](https://doi.org/10.1175/1525-7541(2004)005<0934:SOACSO>2.0.CO;2).
- Chlond, A., O. Böhringer, T. Auerswald, and F. Müller, 2014: The effect of soil moisture and atmospheric conditions on the development of shallow cumulus convection: A coupled large-eddy simulation–land surface model study. *Meteor. Z.*, **23**, 491–510, <https://doi.org/10.1127/metz/2014/0576>.
- Cioni, G., and C. Hohenegger, 2017: Effect of soil moisture on diurnal convection and precipitation in large-eddy simulations. *J. Hydrometeorol.*, **18**, 1885–1903, <https://doi.org/10.1175/JHM-D-16-0241.1>.
- Clark, D. B., and Coauthors, 2011: The Joint UK Land Environment Simulator (JULES), model description – Part 2: Carbon fluxes and vegetation dynamics. *Geosci. Model Dev.*, **4**, 701–722, <https://doi.org/10.5194/gmd-4-701-2011>.
- Cotton, W. R., and Coauthors, 2003: RAMS 2001: Current status and future directions. *Meteor. Atmos. Phys.*, **82**, 5–29, <https://doi.org/10.1007/s00703-001-0584-9>.
- Cox, P. M., R. A. Betts, C. B. Bunton, R. L. H. Essery, P. R. Rowntree, and J. Smith, 1999: The impact of new land surface physics on the GCM simulation of climate and climate sensitivity. *Climate Dyn.*, **15**, 183–203, <https://doi.org/10.1007/s003820050276>.
- Dirmeyer, P. A., and Coauthors, 2012: Simulating the diurnal cycle of rainfall in global climate models: Resolution versus parameterization. *Climate Dyn.*, **39**, 399–418, <https://doi.org/10.1007/s00382-011-1127-9>.
- Drager, A. J., and S. C. van den Heever, 2017: Characterizing convective cold pools. *J. Adv. Model. Earth Syst.*, **9**, 1091–1115, <https://doi.org/10.1002/2016MS000788>.
- , L. D. Grant, and S. C. van den Heever, 2020: Cold pool responses to changes in soil moisture. *J. Adv. Model. Earth Syst.*, **12**, e2019MS001922, <https://doi.org/10.1029/2019MS001922>.
- Ek, M., and L. Mahrt, 1994: Daytime evolution of relative humidity at the boundary layer top. *Mon. Wea. Rev.*, **122**, 2709–2721, [https://doi.org/10.1175/1520-0493\(1994\)122<2709:DEORHA>2.0.CO;2](https://doi.org/10.1175/1520-0493(1994)122<2709:DEORHA>2.0.CO;2).
- Ek, M. B., and A. A. M. Holtslag, 2004: Influence of soil moisture on boundary layer cloud development. *J. Hydrometeorol.*, **5**, 86–99, [https://doi.org/10.1175/1525-7541\(2004\)005<0086:IOSMOB>2.0.CO;2](https://doi.org/10.1175/1525-7541(2004)005<0086:IOSMOB>2.0.CO;2).
- Eltahir, E. A. B., 1998: A soil moisture–rainfall feedback mechanism: 1. Theory and observations. *Water Resour. Res.*, **34**, 765–776, <https://doi.org/10.1029/97WR03499>.
- , and R. L. Bras, 1996: Precipitation recycling. *Rev. Geophys.*, **34**, 367–378, <https://doi.org/10.1029/96RG01927>.
- Findell, K. L., and E. A. B. Eltahir, 1997: An analysis of the soil moisture–rainfall feedback, based on direct observations from Illinois. *Water Resour. Res.*, **33**, 725–735, <https://doi.org/10.1029/96WR03756>.
- , and —, 2003a: Atmospheric controls on soil moisture–boundary layer interactions: Three-dimensional wind effects. *J. Geophys. Res.*, **108**, 8385, <https://doi.org/10.1029/2001JD001515>.
- , and —, 2003b: Atmospheric controls on soil moisture–boundary layer interactions. Part I: Framework development. *J. Hydrometeorol.*, **4**, 552–569, [https://doi.org/10.1175/1525-7541\(2003\)004<0552:ACOSML>2.0.CO;2](https://doi.org/10.1175/1525-7541(2003)004<0552:ACOSML>2.0.CO;2).
- , P. Gentine, B. R. Lintner, and C. Kerr, 2011: Probability of afternoon precipitation in eastern United States and Mexico

- enhanced by high evaporation. *Nat. Geosci.*, **4**, 434–439, <https://doi.org/10.1038/ngeo1174>.
- Ford, T. W., A. D. Rapp, and S. M. Quiring, 2015a: Does afternoon precipitation occur preferentially over dry or wet soils in Oklahoma? *J. Hydrometeorol.*, **16**, 874–888, <https://doi.org/10.1175/JHM-D-14-0005.1>.
- , —, —, and J. Blake, 2015b: Soil moisture–precipitation coupling: Observations from the Oklahoma Mesonet and underlying physical mechanisms. *Hydrol. Earth Syst. Sci.*, **19**, 3617–3631, <https://doi.org/10.5194/hess-19-3617-2015>.
- Gentine, P., A. A. M. Holtzlag, F. D’Andrea, and M. Ek, 2013: Surface and atmospheric controls on the onset of moist convection over land. *J. Hydrometeorol.*, **14**, 1443–1462, <https://doi.org/10.1175/JHM-D-12-0137.1>.
- Gero, A. F., and A. J. Pitman, 2006: The impact of land cover change on a simulated storm event in the Sydney Basin. *J. Appl. Meteor. Climatol.*, **45**, 283–300, <https://doi.org/10.1175/JAM2337.1>.
- Giorgi, F., L. O. Mearns, C. Shields, and L. Mayer, 1996: A regional model study of the importance of local versus remote controls of the 1988 drought and the 1993 flood over the central United States. *J. Climate*, **9**, 1150–1162, [https://doi.org/10.1175/1520-0442\(1996\)009<1150:ARMSOT>2.0.CO;2](https://doi.org/10.1175/1520-0442(1996)009<1150:ARMSOT>2.0.CO;2).
- Goudriaan, J., 1989: Simulation of micrometeorology of crops, some methods and their problems, and a few results. *Agric. For. Meteorol.*, **47**, 239–258, [https://doi.org/10.1016/0168-1923\(89\)90098-1](https://doi.org/10.1016/0168-1923(89)90098-1).
- Grant, L. D., and S. C. van den Heever, 2014: Aerosol-cloud-land surface interactions within tropical sea breeze convection. *J. Geophys. Res. Atmos.*, **119**, 8340–8361, <https://doi.org/10.1002/2014JD021912>.
- , and —, 2016: Cold pool dissipation. *J. Geophys. Res. Atmos.*, **121**, 1138–1155, <https://doi.org/10.1002/2015JD023813>.
- Guillot, B. P., B. Orlowsky, D. G. Miralles, A. J. Teuling, and S. I. Seneviratne, 2015: Reconciling spatial and temporal soil moisture effects on afternoon rainfall. *Nat. Commun.*, **6**, 6443, <https://doi.org/10.1038/ncomms7443>.
- Harrington, J. Y., 1997: The effects of radiative and microphysical processes on simulated warm and transition season Arctic stratus. Atmospheric Science Paper 637, Colorado State University, 289 pp., <https://hdl.handle.net/10217/234498>.
- Hill, G. E., 1974: Factors controlling the size and spacing of cumulus clouds as revealed by numerical experiments. *J. Atmos. Sci.*, **31**, 646–673, [https://doi.org/10.1175/1520-0469\(1974\)031<0646:FCTSAS>2.0.CO;2](https://doi.org/10.1175/1520-0469(1974)031<0646:FCTSAS>2.0.CO;2).
- Hillel, D., 2003: *Introduction to Environmental Soil Physics*. Academic Press, 498 pp., <https://doi.org/10.1016/B978-0-12-348655-4.X5000-X>.
- Hohenegger, C., and B. Stevens, 2018: The role of the permanent wilting point in controlling the spatial distribution of precipitation. *Proc. Natl. Acad. Sci. USA*, **115**, 5692–5697, <https://doi.org/10.1073/pnas.1718842115>.
- , P. Brockhaus, C. S. Bretherton, and C. Schär, 2009: The soil moisture–precipitation feedback in simulations with explicit and parameterized convection. *J. Climate*, **22**, 5003–5020, <https://doi.org/10.1175/2009JCLI2604.1>.
- Kang, S.-L., 2016: Regional Bowen ratio controls on afternoon moist convection: A large eddy simulation study. *J. Geophys. Res. Atmos.*, **121**, 14 056–14 083, <https://doi.org/10.1002/2016JD025567>.
- Koster, R. D., and Coauthors, 2004: Regions of strong coupling between soil moisture and precipitation. *Science*, **305**, 1138–1140, <https://doi.org/10.1126/science.1100217>.
- Kristianti, F., D. Nguyen-Le, and T. J. Yamada, 2018: Effect of soil moisture on shallow cumulus cloud in large eddy simulation. *J. Japan Soc. Civil Eng.*, **74**, I\_33–I\_40, [https://doi.org/10.2208/jscej.74.I\\_33](https://doi.org/10.2208/jscej.74.I_33).
- Lawston, P. M., 2017: Impacts of irrigation on land-atmosphere interactions in high-resolution model simulations. Ph.D. dissertation, University of Delaware, 130 pp., <https://udspace.udel.edu/handle/19716/21229>.
- Lee, T. J., 1992: The impact of vegetation on the atmospheric boundary layer and convective storms. Atmospheric Science Paper 509, Colorado State University, 137 pp., <https://hdl.handle.net/10217/234871>.
- , and R. A. Pielke, 1992: Estimating the soil surface specific humidity. *J. Appl. Meteorol.*, **31**, 480–484, [https://doi.org/10.1175/1520-0450\(1992\)031<0480:ETSSSH>2.0.CO;2](https://doi.org/10.1175/1520-0450(1992)031<0480:ETSSSH>2.0.CO;2).
- Lucas, C., E. J. Zipser, and M. A. LeMone, 1994: Vertical velocity in oceanic convection off Tropical Australia. *J. Atmos. Sci.*, **51**, 3183–3193, [https://doi.org/10.1175/1520-0469\(1994\)051<3183:VVIOCO>2.0.CO;2](https://doi.org/10.1175/1520-0469(1994)051<3183:VVIOCO>2.0.CO;2).
- Meyers, M. P., R. L. Walko, J. Y. Harrington, and W. R. Cotton, 1997: New RAMS cloud microphysics parameterization. Part II: The two-moment scheme. *Atmos. Res.*, **45**, 3–39, [https://doi.org/10.1016/S0169-8095\(97\)00018-5](https://doi.org/10.1016/S0169-8095(97)00018-5).
- Mission Research Corporation, 1997: RAMS technical description. 50 pp., accessed 3 June 2021, <https://raw.githubusercontent.com/RAMSmmodel/RAMS/v6.3.00/docs/RAMS-TechnicalManual.pdf>.
- Mohanty, B. P., and J. Zhu, 2007: Effective hydraulic parameters in horizontally and vertically heterogeneous soils for steady-state land–atmosphere interaction. *J. Hydrometeorol.*, **8**, 715–729, <https://doi.org/10.1175/JHM606.1>.
- Nicolai-Shaw, N., M. Hirschi, H. Mittelbach, and S. I. Seneviratne, 2015: Spatial representativeness of soil moisture using in situ, remote sensing, and land reanalysis data. *J. Geophys. Res. Atmos.*, **120**, 9955–9964, <https://doi.org/10.1002/2015JD023305>.
- NWS, 2009: Categorical. National Weather Service Glossary, accessed 20 January 2021, <https://w1.weather.gov/glossary/index.php?word=Categorical>.
- Oleson, K. W., and Coauthors, 2008: Improvements to the Community Land Model and their impact on the hydrological cycle. *J. Geophys. Res.*, **113**, G01021, <https://doi.org/10.1029/2007JG000563>.
- Park, J. M., S. C. van den Heever, A. L. Igel, L. D. Grant, J. S. Johnson, S. M. Saleeby, S. D. Miller, and J. S. Reid, 2020: Environmental controls on tropical sea breeze convection and resulting aerosol redistribution. *J. Geophys. Res. Atmos.*, **125**, e2019JD031699, <https://doi.org/10.1029/2019JD031699>.
- Philip, J. R., 1957: Evaporation, and moisture and heat fields in the soil. *J. Meteorol.*, **14**, 354–366, [https://doi.org/10.1175/1520-0469\(1957\)014<0354:EAMAHF>2.0.CO;2](https://doi.org/10.1175/1520-0469(1957)014<0354:EAMAHF>2.0.CO;2).
- Powell, T. L., and Coauthors, 2013: Confronting model predictions of carbon fluxes with measurements of Amazon forests subjected to experimental drought. *New Phytol.*, **200**, 350–365, <https://doi.org/10.1111/nph.12390>.
- Ramos da Silva, R., and R. Avissar, 2006: The hydrometeorology of a deforested region of the Amazon Basin. *J. Hydrometeorol.*, **7**, 1028–1042, <https://doi.org/10.1175/JHM537.1>.
- Randall, D., M. Khairoutdinov, A. Arakawa, and W. Grabowski, 2003: Breaking the cloud parameterization deadlock. *Bull. Amer. Meteor. Soc.*, **84**, 1547–1564, <https://doi.org/10.1175/BAMS-84-11-1547>.
- Rio, C., F. Hourdin, J.-Y. Grandpeix, and J.-P. Lafore, 2009: Shifting the diurnal cycle of parameterized deep convection over

- land. *Geophys. Res. Lett.*, **36**, L07809, <https://doi.org/10.1029/2008GL036779>.
- Rodell, M., and Coauthors, 2015: The observed state of the water cycle in the early twenty-first century. *J. Climate*, **28**, 8289–8318, <https://doi.org/10.1175/JCLI-D-14-00555.1>.
- Saleeby, S. M., and W. R. Cotton, 2004: A large-droplet mode and prognostic number concentration of cloud droplets in the Colorado State University Regional Atmospheric Modeling System (RAMS). Part I: Module descriptions and supercell test simulations. *J. Appl. Meteor.*, **43**, 182–195, [https://doi.org/10.1175/1520-0450\(2004\)043<0182:ALMAPN>2.0.CO;2](https://doi.org/10.1175/1520-0450(2004)043<0182:ALMAPN>2.0.CO;2).
- , and —, 2008: A binned approach to cloud-droplet rimming implemented in a bulk microphysics model. *J. Appl. Meteor. Climatol.*, **47**, 694–703, <https://doi.org/10.1175/2007JAMC1664.1>.
- , and S. C. van den Heever, 2013: Developments in the CSU-RAMS aerosol model: Emissions, nucleation, regeneration, deposition, and radiation. *J. Appl. Meteor. Climatol.*, **52**, 2601–2622, <https://doi.org/10.1175/JAMC-D-12-0312.1>.
- Santanello, J. A., and Coauthors, 2018: Land–atmosphere interactions: The LoCo perspective. *Bull. Amer. Meteor. Soc.*, **99**, 1253–1272, <https://doi.org/10.1175/BAMS-D-17-0001.1>.
- Schlemmer, L., C. Hohenegger, J. Schmidli, and C. Schär, 2012: Diurnal equilibrium convection and land surface–atmosphere interactions in an idealized cloud-resolving model. *Quart. J. Roy. Meteor. Soc.*, **138**, 1526–1539, <https://doi.org/10.1002/qj.1892>.
- Schneider, L., C. Barthlott, C. Hoose, and A. I. Barrett, 2019: Relative impact of aerosol, soil moisture, and orography perturbations on deep convection. *Atmos. Chem. Phys.*, **19**, 12343–12359, <https://doi.org/10.5194/acp-19-12343-2019>.
- Smagorinsky, J., 1963: General circulation experiments with the primitive equations I. The basic experiment. *Mon. Wea. Rev.*, **91**, 99–164, [https://doi.org/10.1175/1520-0493\(1963\)091<0099:GCEWTP>2.3.CO;2](https://doi.org/10.1175/1520-0493(1963)091<0099:GCEWTP>2.3.CO;2).
- Stull, R. B., 1988: Boundary conditions and surface forcings. *An Introduction to Boundary Layer Meteorology*, R. B. Stull, Ed., Springer, 251–294.
- Suarez, A., R. Mahmood, A. I. Quintanar, A. Beltrán-Przekurat, and R. Pielke Sr., 2014: A comparison of the MM5 and the Regional Atmospheric Modeling System simulations for land–atmosphere interactions under varying soil moisture. *Tellus*, **66A**, 21486, <https://doi.org/10.3402/tellusa.v66.21486>.
- Taylor, C. M., A. Gounou, F. Guichard, P. P. Harris, R. J. Ellis, F. Couvreux, and M. De Kauwe, 2011: Frequency of Sahelian storm initiation enhanced over mesoscale soil-moisture patterns. *Nat. Geosci.*, **4**, 430–433, <https://doi.org/10.1038/ngeo1173>.
- , R. A. M. de Jeu, F. Guichard, P. P. Harris, and W. A. Dorigo, 2012: Afternoon rain more likely over drier soils. *Nature*, **489**, 423–426, <https://doi.org/10.1038/nature11377>.
- Tuttle, S., and G. Salvucci, 2016: Empirical evidence of contrasting soil moisture–precipitation feedbacks across the United States. *Science*, **352**, 825–828, <https://doi.org/10.1126/science.aaa7185>.
- van den Heever, S. C., S. M. Saleeby, L. D. Grant, A. L. Igel, and S. W. Freeman, 2021: RAMSmodel/RAMS: RAMS release version 6.3.01. Zenodo, <https://doi.org/10.5281/zenodo.4143887>.
- Walko, R. L., and Coauthors, 2000: Coupled atmosphere–biophysics–hydrology models for environmental modeling. *J. Appl. Meteor.*, **39**, 931–944, [https://doi.org/10.1175/1520-0450\(2000\)039<0931:CABHMF>2.0.CO;2](https://doi.org/10.1175/1520-0450(2000)039<0931:CABHMF>2.0.CO;2).
- , and C. J. Tremback, 2005: Modifications for the transition from LEAF-2 to LEAF-3. ATMET, LLC, 13 pp., accessed 27 May 2021, <https://raw.githubusercontent.com/RAMSmodel/RAMS/main/docs/RAMS-Leaf2-to-Leaf3.pdf>.
- White, M. A., P. E. Thornton, S. W. Running, and R. R. Nemani, 2000: Parameterization and sensitivity analysis of the BIOME–BGC terrestrial ecosystem model: Net primary production controls. *Earth Interact.*, **4**, [https://doi.org/10.1175/1087-3562\(2000\)004<0003:PASAOT>2.0.CO;2](https://doi.org/10.1175/1087-3562(2000)004<0003:PASAOT>2.0.CO;2).
- Williams, E., and S. Stanfill, 2002: The physical origin of the land–ocean contrast in lightning activity. *C. R. Phys.*, **3**, 1277–1292, [https://doi.org/10.1016/S1631-0705\(02\)01407-X](https://doi.org/10.1016/S1631-0705(02)01407-X).
- Williams, P. D., 2009: A proposed modification to the Robert–Asselin time filter. *Mon. Wea. Rev.*, **137**, 2538–2546, <https://doi.org/10.1175/2009MWR2724.1>.
- Yuan, S., Y. Wang, S. M. Quiring, T. W. Ford, and A. L. Houston, 2020: A sensitivity study on the response of convection initiation to in situ soil moisture in the central United States. *Climate Dyn.*, **54**, 2013–2028, <https://doi.org/10.1007/s00382-019-05098-0>.